IEEE Access
Multidisciplinary | Rapid Review | Open Access Journal

Received March 13, 2021, accepted April 2, 2021, date of publication April 19, 2021, date of current version April 29, 2021.

Digital Object Identifier 10.1109/ACCESS.2021.3073903

Pansharpening PRISMA Data for Marine Plastic Litter Detection Using Plastic Indexes

MARIA KREMEZI[1], VIKTORIA KRISTOLLARI[1], VASSILIA KARATHANASSI[1], KONSTANTINOS TOPOUZELIS[2], (Member, IEEE), POL KOLOKOUSSIS[1], NICOLÒ TAGGIO[3], ANTONELLO AIELLO[3], GIULIO CERIOLA[3], ENRICO BARBONE[4], AND PAOLO CORRADI[5]

[1]Laboratory of Remote Sensing, School of Rural and Surveying Engineering, National Technical University of Athens, 15780 Zografou, Greece
[2]Department of Marine Sciences, University of the Aegean, 81100 Mytilene, Greece
[3]Planetek Italia s.r.l., 70132 Bari, Italy
[4]Regional Agency for the Prevention and Protection of the Environment (ARPA Puglia), 70126 Bari, Italy
[5]Mechatronics and Optics Division, Optics Section, European Space Research and Technology Centre (ESTEC), European Space Agency, 2200 Noordwijk, The Netherlands

Corresponding author: Vassilia Karathanassi (karathan@survey.ntua.gr)

This work was supported in part by the Discovery Element of the European Space Agency's Basic Activities (ESA) under Contract 4000131235/20/NL/GLC, and in part by the Discovery Element of the European Space Agency's Basic Activities, Project: "Plastic Litter Project: Detection and monitoring of artificial plastic targets with satellite imagery and UAV" (ESA) under Contract 4000131040/20/NL/GLC.

ABSTRACT Hyperspectral PRISMA images are new and have not yet been evaluated for their ability to detect marine plastic litter. The hyperspectral PRISMA images have a fine spectral resolution, however, their spatial resolution is not high enough to enable the discrimination of small plastic objects in the ocean. Pansharpening with the panchromatic data enhances their spatial resolution and makes their detection capabilities a technological challenge. This study exploits, for the first time, the potential of using satellite hyperspectral data in detecting small-sized marine plastic litter. Controlled experiments with plastic targets of various sizes constructed from several materials have been conducted. The required pre-processing steps have been defined and 13 pansharpening methods have been applied and evaluated for their ability to spectrally discriminate plastics from water. Among them, the PCA-based substitution efficiently separates plastic spectra from water without producing duplicate edges, or pixelation. Plastic targets with size equivalent to 8% of the original hyperspectral image pixel coverage are easily detected. The same targets can also be observed in the panchromatic image, however, they cannot be detected solely by the panchromatic information as they are confused with other appearances. Exploiting spectra derived from the pan-sharpened hyperspectral images, an index combining methodology has been developed, which enables the detection of plastic objects. Although spectra of plastic materials present similarities with water spectra, some spectral characteristics can be utilized for producing marine plastic litter indexes. Based on these indexes, the index combining methodology has successfully detected the plastic targets and differentiated them from other materials.

INDEX TERMS PRISMA satellite data, hyperspectral imaging, pansharpening, marine pollution, plastic litter detection, indexes, controlled experiments, spectral analysis, image denoising.

I. INTRODUCTION

Oceans receive solid waste from anthropogenic activities [1]. Human heavy reliance on plastic materials is creating a visible and even pervasive "plastic footprint" in the environment. Plastic fragments, lolly sticks, plastic caps/lids, and string/cord (diameter $<$ 1 cm) are the most frequent debris and their amount in the oceans and coastal areas, which is steadily increasing, is now a global major environmental problem [2]. Accumulation of marine debris poses considerable threats to the livelihood of aquatic species and ecosystems, as well as to human beings since microplastics infiltrate

The associate editor coordinating the review of this manuscript and approving it for publication was Qiangqiang Yuan.

the diet of marine and flying organisms and eventually our food chain [3]. Moreover, plastic debris in the oceans is a vector for both organic pollutants [4] and harmful microalgal assemblages [5]. Substantial waste detection, monitoring, and management challenges are faced with regard to plastic litter [6]. At the global scale, the 2030 Agenda for Sustainable Development, adopted by the United Nations in 2015 [7], calls to conserve and sustainably use the oceans, seas, and marine resources with the Sustainable Development Goal No. 14. Among the SDG 14 targets, the 14.1 calls to prevent and significantly reduce marine pollution of all kinds, in particular from land-based activities, including marine debris and nutrient pollution. From the European perspective, the Marine Strategy Framework Directive (MSFD) requires the EU Member States to ensure that ''properties and quantities of marine litter do not cause harm to the coastal and marine environment'' [8].

Despite encouraging results of initial experiments on the detection of large-sized marine debris, overall, marine debris monitoring represents a significant technological challenge. In [9] it was shown that machine learning techniques when applied on Worldview-3 images of 0.3 to 1.2 m spatial resolution, efficiently detect Expanded Polystyrene (EPS) and Anthropogenic Marine Debris (AMD) mixtures deposited on three beaches of Chiloé island. However, it was noted that the inclusion of other ranges of wavelengths may enable the detection of plastic objects in adverse weather conditions, as well as the distinction of types of waste in AMD mixtures other than EPS. In [10] spectral at-sensor properties derived from airborne SASI SWIR imagery with pixel size 0.5 m $\times$ 1.2 m were employed for the distinction of ocean plastics from surrounding seawater using the unique absorption features of polymers. The authors used a reference spectral library of several polymer types to identify the plastic type of a large-sized ghost net for which spectral information from 11 SWIR pixels had been previously retrieved. The study showed the influence of seawater on ocean plastic spectra. Although common absorption features with the library's reference spectra and other hydrocarbons around 1215 and 1732 nm were observed, ocean plastic spectra presented weak similarities with reference spectra. Furthermore, the authors highlighted the need to further investigate the size distribution of observed pieces in relation to the pixel size, although theoretically, there is potential in detecting particles with a size equivalent to the simulated 5% pixel coverage.

In [11] the spectral properties of three artificial floating plastic targets, as well as the surrounding seawater using Sentinel-1 and Sentinel-2 imagery, were investigated. These floating targets consisted of 10 m $\times$ 10 m PET-11.5 L water bottles, LDPE plastic bags, and nylon fishing ghost nets. The authors provided reasonable evidence that both Synthetic Aperture Radar (SAR) and optical imagery have potential application in detecting floating plastics in the marine litter; however, they asserted that the identification of the plastic types and shapes requires multi- to hyper-spectral imaging. In a follow-up experiment [12], artificial targets in 6 Sentinel-2 images in combination with UAV optical data were examined. Spectral unmixing and matched filtering process followed for classifying the pixels containing plastics. The methodology revealed promising results. Plastic litter targets were successfully identified when the plastic coverage of the Sentinel-2 images was larger than 25%. In [13] the coastal waters of Ghana, North-West America, Vietnam, and the east coast of Scotland were selected as case studies based on persistent or acute incidences of marine plastic litter reported in the scientific literature, popular press, and social media. The authors developed the Floating Debris Index (FDI), which allows detecting materials floating on the ocean surface at sub-pixel scales in Sentinel-2 images. Then, they applied the Naïve Bayes algorithm on FDI, NDVI, and atmospherically corrected Sentinel-2 images to compute the probability of a detected pixel belonging to each of the following classes: seaweed; spume; timber; macroplastics; and seawater. The detected pixels were assigned to the class with the highest probability. Candidate plastics were successfully classified as plastics with an accuracy of 86%.

In [14] the authors employed WorldView-2, Advanced Spaceborne Thermal Emission and Reflection Radiometer (ASTER), and SAR satellite datasets for monitoring marine plastic debris events after the great east Japan earthquake in March 2011, when a remarkable amount of $>$1.5 million tons of debris was generated. They employed satellite imagery to monitor plastic pathways and concluded that high spatial resolution satellite tracking reveals faster floating debris motions than expected and invigorated plume evolution within these regions. The same conclusion was drawn in [15] where high-resolution multispectral satellite imagery was used for the efficient monitoring of marine litter dynamics and the detection of its origin. The study also focused on the detection of the dominant marine plastic pathways. The authors detected and verified multiple floating plastic debris incidents using Planet, Sentinel-2, and Landsat-8 data by systematically assessing the spectral signatures from pure floating plastics and discriminating them from other floating features on the sea surface such as sargassum, foam, etc.

Research has indicated that the key requirements needed by remote sensing techniques for improving the capability to detect the spectral signature characteristics associated with plastics, and even theoretically being able to discriminate between different polymers, are high spatial and spectral resolutions. So far, due to the technical and physical limitations of satellite sensors, there are critical trade-offs between the spectral and spatial resolution of satellite imagery. Data of high spectral resolution are characterized by low spatial resolution and vice versa. Nevertheless, the plastic crisis stresses the need to increase the current satellite observing systems' potentials for marine plastic pollution detection and monitoring. Towards optimizing current observing systems' potentials for marine plastic pollution datasets to detect and identify plastics in marine litter, in this study, we evaluate several pansharpening methods on the new hyperspectral data provided by the PRISMA satellite and we propose indexes

to detect plastic objects efficiently. Medium resolution (30 m × 30 m) PRISMA hyperspectral images cover a wide spectral range and have a fine spectral resolution (bandwidth <= 12 nm). Pansharpening with PRISMA panchromatic band could increase the hyperspectral data spatial resolution to 5 m × 5 m and their potentials for detecting plastic debris in finer scales. The study focuses on the detection of small-sized plastic targets (≤5 m), which makes this research even more challenging. Through controlled experiments with various plastic target sizes, it contributes to investigating the undermost size of the observed targets in relation to the pixel size, as well as the way that the seawater influences the ocean plastic litter spectra. Finally, the study highlights the required pre-processing steps and contributes to evaluating the images provided by the recent hyperspectral PRISMA mission for marine litter detection. It is worth noting that not only PRISMA data but also satellite hyperspectral data are being evaluated for the first time for their potentials in detecting plastic litter.

II. PANSHARPENING METHODS

Pansharpening of hyperspectral (HS) images is still an open issue. So far, only a few methods have been presented in the literature to address it, the majority of which has been developed in order to fuse panchromatic (PAN) and multispectral (MS) data or MS and HS data acquired on a similar spectral range. However, with the increasing availability of HS systems, the pansharpening methods have been extended to the fusion of HS and PAN images. The arisen difficulty consists in defining a fusion model that yields good performance in the part of the HS spectral range that is not covered by PAN data, in which the high spatial resolution information is missing [16]. In the last decades, a variety of pansharpening techniques have been developed. Most of them can be roughly classified into five categories: component substitution (CS); multiresolution analysis (MRA); hybrid; Bayesian; and deep learning (DL) methods.

In the CS approach, a component of the HS image is substituted with the PAN image. These methods rely upon the higher spectral resolution image's projection into another space to separate spatial and spectral information. Subsequently, the component that contains the spatial information is substituted with the PAN image and the sharpened data are projected back to the original space [16]. A well-known CS method exploits the Principal Component Analysis (PCA). Other CS methods are the Gram–Schmidt (GS) and the GS Adaptive (GSA) methods [17]. The GS method begins with the creation of the low resolution (LR) PAN image by averaging the bands of the HS image. Then, a complete orthogonal decomposition (GS transformation) is performed on the created LR PAN image together with the HS image, where the former is the first component. Histogram matching is applied on the original PAN image to match the simulated one and then the modified PAN image substitutes the first component of the transformed image. The pan-sharpened image is procured by inverting the decomposition. In [17] the GSA method was proposed, which is an enhanced version of GS. In this method, the simulated PAN image is generated by the weighted average of the HS bands.

In the MRA approach spatial details extracted from the PAN image through a multiresolution analysis are injected into the upsampled HS bands. The concept of this pansharpening category can be described with the formula below (1):

$$\mathbf{F} = \widetilde{\mathbf{HS}} + \mathbf{G} \otimes (\mathbf{P} - \mathbf{P}_{\mathrm{LP}}) \tag{1}$$

where $\mathbf{F}$ is the pan-sharpened result, $\widetilde{\mathbf{HS}}$ is the interpolated HS image, $\mathbf{G}$ are the gain coefficients, $\mathbf{P}$ is the PAN image, $\mathbf{P}_{\mathrm{LP}}$ is the low-pass version of $\mathbf{P}$, and the symbol $\otimes$ denotes element-wise multiplication.

The steps of this approach are: 1) interpolating the HS image to the scale of the $\mathbf{P}$ image; 2) calculating a low-pass version of PAN; 3) computing the gain coefficients, and 4) injecting the extracted details into the interpolated HS image. The gain coefficients are most commonly either a matrix with all cells equal to 1 (additive injection scheme) or are calculated by (2):

$$\mathbf{G} = \widetilde{\mathbf{HS}} \oslash \mathbf{P}_{\mathrm{LP}} \tag{2}$$

where the symbol $\oslash$ denotes element-wise division.

This is the high pass modulation (HPM) or multiplicative injection scheme, where the local intensity contrast of the PAN image is injected into the fused image. A well-known method of this category is the Smoothing Filter-based Intensity Modulation (SFIM) algorithm [18], where the low pass version of the PAN image is calculated by the application of a single linear time-invariant low pass filter to the PAN image and the injection scheme is the HPM. Other MRA methods are based on the pyramidal decomposition, where the low-pass filtering of the PAN image is done in more than one step [19]. A Gaussian filter is applied in each level and the differences between consecutive levels define the Laplacian pyramid. The Gaussian filter is used because it is most suitable to match the sensor's Modulation Transfer Function (MTF), which allows extracting details from the PAN image that are not visible in the HS image due to its spatial resolution. Then, either the additive or multiplicative injection scheme could be used, resulting in the MTF-Generalized Laplacian Pyramid (MTF-GLP) or the MTF-GLP High Pass Modulation (MTF-GLP-HPM) method, respectively. Local mean matching (LMM) and local mean and variance matching (LMVM) filters [20] also belong to the MRA pansharpening approach. They are designed to minimize the difference between the fused image and the low-resolution HS bands, so they preserve most of the HS image's spectral information.

The hybrid approach uses concepts from the CS and MRA-based methods. Since CS methods are known for preserving the spatial information but generating spectral distortion, whereas MRA methods preserve the spectral information but may have some spatial blur, hybrid methods have been created to find a balance between spectral and spatial preservation. Such a method is the Guided Filter PCA (GFPCA) [21]. In this method, PCA is applied to the

HS image to decorrelate the bands and separate the noise from the signal. Instead of substituting the first component with the PAN image, the first k PCA bands with the most information are upsampled by applying a guided filter technique. The rest of the PCA bands are simply interpolated by cubic interpolation. Then, the inverse PCA is performed to obtain the pan-sharpened image.

The Bayesian approach utilizes knowledge modeling through an appropriate distribution to solve the probabilistic framework that results in the pan-sharpened HS image. The main idea of the Bayesian methods is to see the PAN image as the spatial degradation of the result we want to restore and the HS image as its spectral degradation. A good modeling knowledge of those degradations is needed to reverse them to restore the fused image. The Naïve Gaussian prior method (BayesNaive) [22] utilizes the Markov chain Monte Carlo (MCMC) method to infer the pan-sharpened image from its posterior distribution. The HySure [23] method can also be classified into this category as it proposes a form of vector total variation (VTV) for the regularizer, and the pan-sharpened image is the solution of an optimization problem.

Recent research in pansharpening involves deep learning approaches based on convolutional neural networks (CNNs). In this study, three CNNs have been applied. The first two followed a supervised approach and were trained using the Keras library [24] (backend: Tensorflow [25]). The third followed an unsupervised approach and was trained using the Pytorch [26] library.

The first DL method (PNN) was based on a three-layer architecture proposed in [27] for the pansharpening of very high resolution (VHR) multispectral satellite images. The first convolutional layer computes 64 feature maps using a 9 px × 9 px receptive field (patch size) and the second computes 32 feature maps with a 5 px × 5 px kernel size. Rectified Linear Unit (ReLU) was used as an activation function in the hidden layers while the identity function was used in the output layer with a 5 px × 5 px kernel size. The backpropagation process was implemented according to the Adaptive moment estimation (Adam) method [28]. The spatial resolution of the input and output of the network was defined according to Wald's protocol. In more detail, for the study needs the network was trained on an input that resulted from concatenating: i) the panchromatic (PAN) image (original spatial resolution: 5 m) downsampled to the spatial resolution of the HS image, which for PRISMA corresponds to 30 m; and ii) the HS image downsampled by the same ratio, i.e. 1/6 to 180 m and then upsampled to its original size. The original HS image was fed to the network as an output. Thus, the trained CNN is expected to approximate the function that upscales a PRISMA HS image by the ratio mentioned above. During the inference stage, the pan-sharpened image (spatial resolution: 5 m) was created by feeding the network with an input that results from concatenating: i) the original PAN image; and ii) the original HS image upsampled to the size of the original PAN. The training was performed on a PRISMA image acquired on 18/09/2020 (size: 1000 px × 1000 px) on ∼60000 patches (size: 9 px × 9 px) and lasted for ∼6 hours (160 epochs, batch size:128). For the pansharpening of any other PRISMA image, a fine-tuning process is required. In this study, the fine-tuning process lasted for ∼1 hour. Fine-tuning was considered necessary since the radiance values differ between different acquisition dates. It is noted that this CNN, besides being trained on the original bands, was also trained on values produced after clipping 1% of the histogram values for each band (left and right) to prevent lower performance due to sparse extreme values.

The second DL method (CAE) was based on the architecture proposed in [29] for the pansharpening of VHR multispectral satellite images. The architecture is composed of an encoder and a symmetric decoder. The encoder consists of three convolutional layers and two pooling layers. The decoder consists of three convolutional layers and two upsampling layers. To enhance performance, for the purpose of the pansharpening of the PRISMA images, skip connections were added between the encoding and the decoding part. Rectified Linear Unit (ReLU) was used as an activation function in the hidden layers while the identity function was used in the output layer. The backpropagation process was implemented according to the Adam method. The spatial resolution of the input and output of the network was defined according to Wald's protocol. For the current study, the network was trained on an input that resulted from downsampling the PAN image from 5 m to 30 m (ratio: 1/6) and then upsampling it to its original size (6000 px × 6000 px). The original PAN image was fed to the network as an output. During the inference stage, the pan-sharpened image (spatial resolution: 5 m) was created by feeding the network with the upsampled HS bands to the size of the original PAN. The HS bands were fed to the network one by one. The training was performed on the PAN band of a PRISMA image acquired on 18/09/2020 on ∼1.5 million patches (size: 8 px × 8 px) and lasted for ∼5 hours (150 epochs, batch size: 128).

For the third DL method, the guided deep decoder (GDD) proposed in [30] was applied. GDD is composed of an encoder-decoder network with skip connections and a deep decoder network. The encoder-decoder network is similar to the architecture of U-net [31] and produces the features of a guidance image at multiple scales. The network introduces an upsampling refinement unit (URU) and a feature refinement unit (FRU) to promote similar spatial locality and semantic alignment with the features of the guidance image. The proposed loss function is presented below (3):

$$L = \mu \left\| \widetilde{\mathbf{X}_\mathbf{S}} - \widetilde{\mathbf{Y}} \right\|_F^2 + \left| \mathbf{D}\nabla\widetilde{\mathbf{X}} - \nabla\widetilde{\mathbf{G}} \right| \tag{3}$$

where $\widetilde{\mathbf{X}}$ is the output pan-sharpened image, $\widetilde{\mathbf{Y}}$ is the HS input image, $\widetilde{\mathbf{G}}$ is the PAN input image expanded to the same number of bands of $\widetilde{\mathbf{X}}$, $\nabla\widetilde{\mathbf{X}}$ is the image gradient of $\widetilde{\mathbf{X}}$, $\nabla\widetilde{\mathbf{G}}$ is the image gradient of $\widetilde{\mathbf{G}}$, $\widetilde{\mathbf{X}_\mathbf{S}}$ is the spatially downsampled $\widetilde{\mathbf{X}}$, $\mathbf{D}$ is the diagonal matrix to weight each channel of $\nabla\widetilde{\mathbf{X}}$ so that the magnitude of $\widetilde{\mathbf{X}}$ is scaled to that of $\nabla\widetilde{\mathbf{G}}$, μ is a

scalar controlling the balance between the two terms, $\|\cdot\|_F$ is the Frobenius norm, and $|\cdot|$ is the l_1 norm.

This network was tested on a PRISMA image acquired on 18/09/2020. A segment of the PAN band with size 210 px × 200 px represented the guidance image. The input HS segment corresponding to the same region (35 px × 33 px) was fed to the model in seven separate groups because of memory limitation, resulting in seven separate trainings. Each training lasted for ∼20 min (6000 iterations). The final pansharpened image was created by concatenating the partial output images. It has to be noted that the acronyms used for the three DL approaches were acquired from the respective studies.

III. FIELD CAMPAIGNS: DATA ACQUISITION AND PROCESSING

The controlled experiments took place in the area of Tsamakia beach, in the coastal region of Lesvos island, Greece. The selected area offers plenty of unobstructed space guarantying the construction, deployment, and storing of targets during the experiments, and it does not hinder any touristic or commercial activities. Additionally, Tsamakia beach waters are sufficiently deep and the seabed offers a dark substrate that efficiently simulates deep waters.

For the experiment needs, 12 floating plastic targets were constructed in total. Their size was selected according to the spatial resolution of PRISMA which is expected to be achieved by pansharpening techniques, i.e. 5.1 m × 5.1 m (similar to the resolution of PRISMA fused data), 2.4 m × 2.4 m (nearly half of the resolution of PRISMA fused data), and 0.6 m × 0.6 m (about 1/8 of the resolution of PRISMA fused data). For each one of these three different sizes of targets, four types/compositions of plastic materials with various colors were set up (Fig. 1): 1) High-density polyethylene (HDPE) (tarps in white, yellow and green color); 2) Polyethylene Terephthalate (PET) (transparent water bottles and green oil bottles); 3) Polystyrene (PS) (sheets for building insulation in cyan color); and 4) all the above materials in equal surface extent. HDPE as well as LDPE (low-density polyethylene) and PP (polypropylene) are used to make common household items such as milk jugs, plastic bags, and drinking straws. These materials have less density than seawater, causing them to float on the sea surface. PET, PVC (polyvinyl chloride), and PS are denser than seawater. They are usually observed on beaches and will most likely float on coastal seawater or close to ships before sinking and litter the seabed.

The analysis was performed on two clear sky PRISMA images collected on 18th September 2020 and 22nd October 2020. On the dates that the satellite passed over the test area, offshore deployment of the targets was carried out. A series of steel and cement anchors were used for the offshore deployment of the targets. The anchors were set above dark patches of the seafloor to minimize the reflectance contribution of a bright seafloor. The targets were deployed at a distance of 30 m from each other, to minimize the possibility that more than one target would be captured

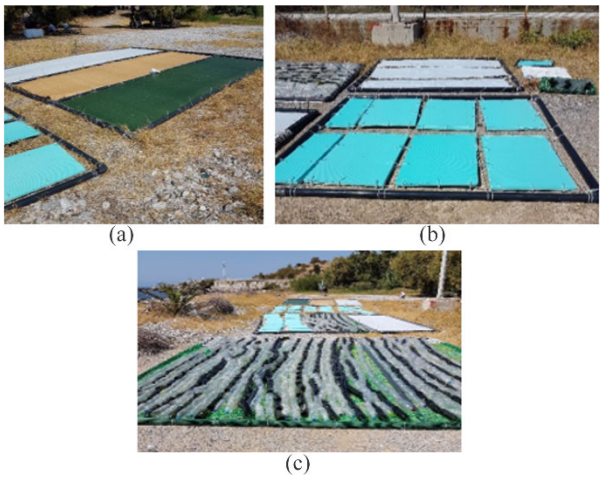

FIGURE 1. The targets. (a) Focus set on HDPE. (b) Focus set on PS. (c) Focus set on PET.

in the same PRISMA pixel. They were set at varying sea depths due to area restrictions. Larger targets were set deeper (∼12 m depth) than smaller targets (∼2 m depth) (Fig. 2). GPS instruments were attached to four of the targets used. In addition, on the experiments' dates, close-range RGB images were acquired using the on-board camera of a DJI Phantom 4 Pro V2.0 UAV. These images were orthorectified (Fig. 2) using the Agisoft Metashape software [32]. The spatial resolution of the orthophotos was around 2.5 cm depending on the flight height. In this resolution all the targets are well distinguished. However, the four 0.6 m × 0.6 m targets are not distinguishable at the scale of Fig. 2.

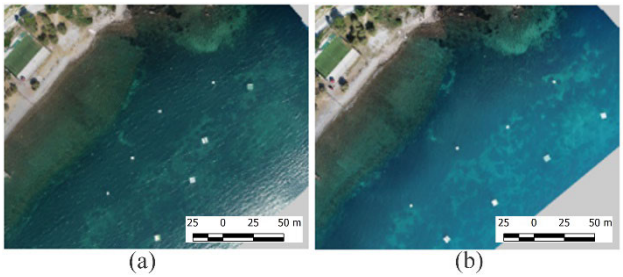

FIGURE 2. Orthophoto image of the targets offshore. (a) Date: 18/09/2020. (b) Date: 22/10/2020.

PRISMA hyperspectral (HS) imagery includes 234 bands (400-2500 nm) at a spatial resolution of 30 m. Additionally, PRISMA Panchromatic (PAN) imagery (400-700 nm) is provided at a spatial resolution of 5 m. The PAN data is co-registered with the HS data to permit the testing of image fusion techniques. For the study needs, both level 1 (L1) and level 2d (L2D) PRISMA products were analyzed. Because atmospheric correction over water areas affects image radiometry, pansharpening was decided to be carried out using the L1 products. Regarding pre-processing, it was decided to avoid applying an atmospheric correction to the HS image to mitigate errors that could arise from any correction scheme. The available L1 products presented a slight

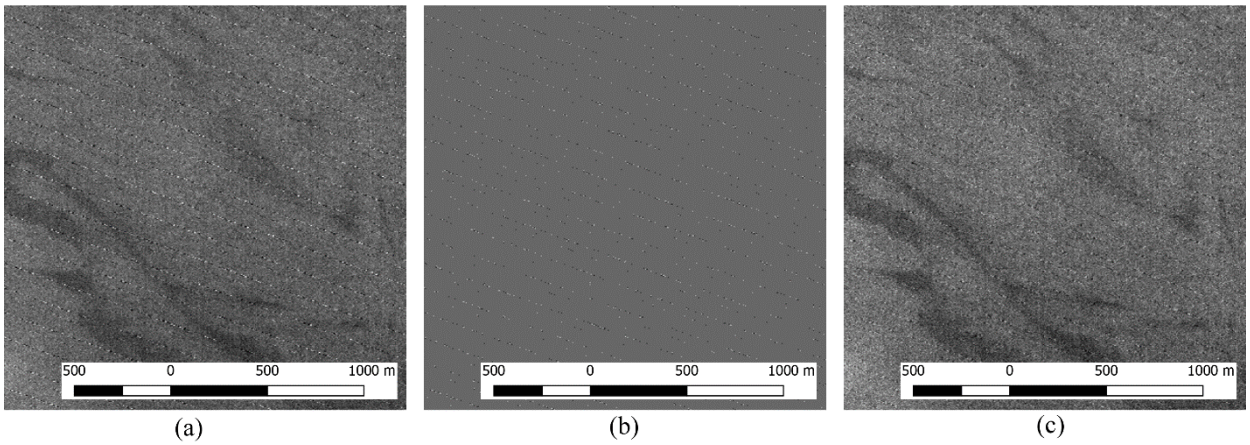

FIGURE 3. Zoomed in water PAN image. (a) Before the noise reduction. (b) High-pass Gaussian result. (c) After the noise reduction.

misalignment between the HS and the PAN image; thus, fine co-registration between the two datasets was initially carried out. Finally, in the PAN images, a linear periodic noise was observed in water areas where the radiance values measured by the sensor are considerably low compared to land areas.

Elimination of such noise is usually accomplished by Fourier filtering where the image is decomposed into frequency waves by a 2D Fourier transformation and then filtering of specific frequencies (discrete spikes) takes place on the frequency domain of the magnitude. However, in PRISMA images, such spikes were not observed for two reasons: 1) the linear noise presented in the image contains both high- and low-intensity values; and 2) the lines are not continuous and present various spacing among them. Moreover, the spatial frequency of the linear pattern is not constant. Thus, a new method was developed. Firstly, a high- pass Gaussian filter was applied on the PAN image, which amplifies the noise and produces an image with gray pixels (zero value) for the non-noisy pixels of the original PAN image (Fig. 3) and with bright or dark pixels for the noisy pixels. This process highlights pixels that present different values from their neighbors, including pixels that present plastic targets. Then, the linear noise's inclination and the number of the highlighted pixels that lay on lines having such an inclination are calculated.

If the number of the highlighted pixels exceeds a threshold for each line, then the algorithm assigns the mean value of water pixels to the highlighted pixels. This method does not eliminate the linear noise with 100% accuracy; however, the low number of bright residuals slightly affects the plastic detection process. Although around 10% of the noisy pixels remain, their intensity values are closer to those of the water pixels.

A variety of pansharpening methods were then applied to the PRISMA data to procure an HS image with better spatial resolution. These methods were briefly described in the previous section. Before pansharpening, bands with low signal-to-noise-ratio were excluded from the data resulting in an HS image with 175 bands. The bands that were removed were in the intervals 1350-1470 nm and 1800-1950 nm. In these spectral regions, water vapor absorbs much of the incident solar radiation.

IV. PANSHARPENING RESULTS AND EVALUATION

Pansharpening methods were initially evaluated for their ability to discriminate the plastic targets from water. In Fig. 4, 5, the spectral signatures of the plastic targets and various water samples (the same for every image) are shown for the original HS image and each pan-sharpened result in blue color. The various plastic materials are shown in different colors although their identification is not of interest at this point. Water vapor absorption at (720, 820, 940, and 1120) nm and molecular oxygen absorption at 760–770 nm are easily observed in all the signatures. The plastic targets and random spectral signatures of water pixels show that target and water spectra have a similar shape but the spectra of the targets present higher radiance values, except for a few water spectra corresponding to water pixels near the shore. In Table 1 similarity measurements (spectral angle distance (SAD) and the correlation coefficient (CC)) between water and plastic target spectra are shown. The min, max, and, mean values of SAD and CC measurements between plastic spectral signatures and water spectral signatures are indicated for the original image and the pan-sharpened results. It is observed that: 1) in the original image, water and plastic signatures are significantly correlated; and 2) in all the pansharpening methods, signatures present low SAD values and high CC values. The latter demonstrates the spectra similarity between water and plastics. Pansharpening methods which exhibit the highest mean SAD values and the lowest mean CC values are the most appropriate for marine plastic discrimination.

Based on Table 1 and Fig. 4, 5, it is concluded that the component substitution methods such as PCA, GS, and GSA yield the best results. Plastic spectra present quite higher radiance values than water, while similarity values between water and plastic targets are the smallest. Three MRA methods, the Smoothing Filter-based Intensity Modulation (SFIM) method, the MTF-GLP and the MTF-GLP-HPM also present

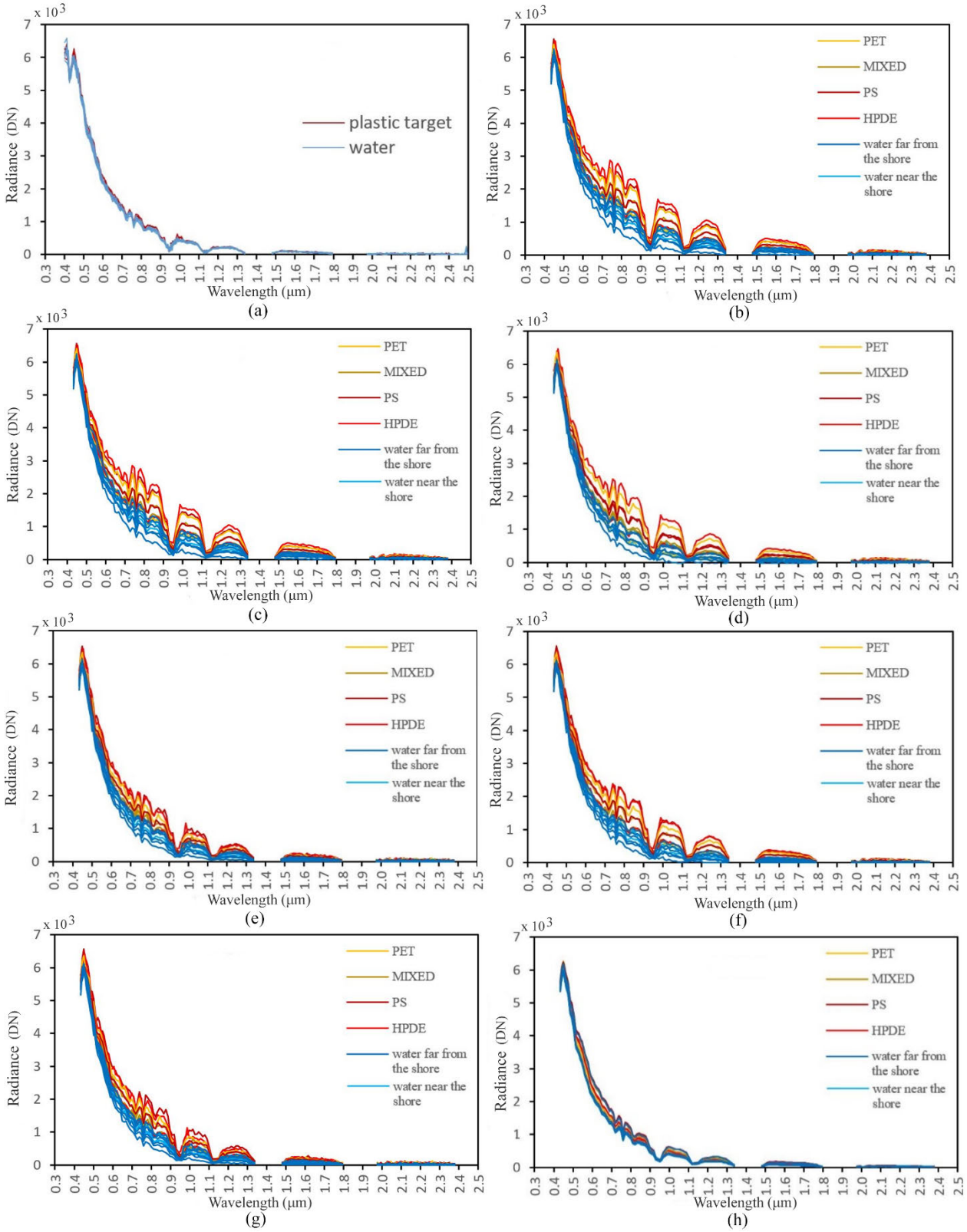

FIGURE 4. Spectral signatures of water and plastic targets. (a) Original HS image (30 m spatial resolution). (b) PCA. (c) GS. (d) GSA. (e) SFIM. (f) MTF-GLP. (g) MTF-GLP-HPM. (h) GFPCA.

TABLE 1. Similarity measurements between water pixels and plastic target spectra.

	SAD (rad)			CC		
	min	max	mean	min	max	mean
Original HS image	0.026690	0.052040	0.039209	0.998348	0.999545	0.999036
PCA	0.022155	0.361378	**0.137439**	**0.942857**	0.999646	**0.988574**
GS	0.022306	0.358058	0.136646	0.944418	0.999643	0.988811
GSA	**0.026358**	0.372364	0.131318	0.945684	0.999558	0.990175
SFIM	0.026099	0.245734	0.096315	0.974023	0.999536	0.994593
MTF-GLP	0.024633	0.327536	0.134929	0.956624	0.999588	0.990092
MTF-GLP-HPM	0.026200	0.262613	0.101668	0.970225	0.999531	0.994001
LMM	0.005229	0.041735	0.019314	0.999155	0.999982	0.999750
LMVM	0.010859	0.106932	0.048492	0.996401	0.999929	0.998860
GFPCA	0.003576	0.088835	0.031062	0.996457	0.999991	0.999300
BayesNaive	0.018312	0.130884	0.060868	0.993126	0.999778	0.997962
HySure	0.001423	0.043559	0.014458	0.998976	0.999999	0.999847
PNN	0.005967	0.060582	0.030452	0.998096	0.999982	0.999426
PNN – histogram clipping	0.019818	0.300965	**0.139743**	**0.940634**	0.999745	**0.984474**
CAE	0.020642	0.087132	0.042123	0.995322	0.999715	0.998774
GDD	0.023663	0.081706	0.045095	0.995933	0.999643	0.998632

satisfactory results, whereas Hybrid and Bayesian methods did not achieve to sufficiently discriminate plastic target spectra from water spectra. The spectra derived by the Bayesian methods have different shapes compared to the respective original spectra, generating significant spectral distortions. As far as the deep learning methods are concerned, only the PNN trained on values produced after histogram clipping showed good separation of the random water spectra from the target spectra.

In terms of spatial distortions, only PCA and GS methods produce clear edge results. The results of MRA and hybrid methods seem blurry and duplicate edges are observed along the shoreline and port piers. These drawbacks are caused by the high pass detail injection and may be emphasized by misregistration between HS and PAN data. Bayesian methods produce blurry results with a noise pattern and DL methods present pixelated/blurry outputs. The less satisfactory results, provided by the DL methods, can be explained mostly by the large difference between the spatial resolutions of the PAN and the HS bands as, objects depicted in 5 m spatial resolution images present much more spatial information (e.g. visible edges) in comparison to what is depicted on a 30 m resolution image. Thus, the problem is much more challenging than e.g. recreating 0.5 m spatial resolution from 2 m, which is the usual case in the majority of the DL pansharpening studies encountered in the scientific literature. Other reasons are the unavailability of HS ground-truth data with 5 m spatial resolution during training and the fact that there is no spectral overlap between the panchromatic band and the NIR-SWIR bands. Fig. 6 shows the outputs for four pansharpening methods (PCA, SFIM, BayesNaive, PNN – histogram clipping) for the image acquired on 18/9/2020.

Since PCA is the simplest method, it could be selected as the most efficient method for our study. In Fig. 7, the PCA results of the image acquired on 18/9/2020 are shown along with the panchromatic band. The targets are highlighted in color. It is observed that all the medium and large-sized targets except for those containing PET material, are easily discriminated in the pan-sharpened image.

V. PLASTIC LITTER INDEXES

Marine litter indexes are simple mathematical formulas that rely on discriminative features for detecting marine plastics. Indexes found in the literature, such as the hydrocarbon index [33], the Sentinel-2-based index [34], and the Floating Debris Index (FDI) [13] were tested on the PCA-based pan-sharpened image. Especially, the hydrocarbon index was tested for 19 different band combinations. From all the aforementioned indexes, only the combination of (866, 951, and 1240 nm) bands in the hydrocarbon index yielded satisfactory results. However, even in this case, spectral signatures of mixed and PET targets were confused with those of water near the shore. Moderate performance of the existing indexes is due to the fact that absorption features of plastic material are smoothed in PRISMA imagery. The water abundance within the pixel coverage of the HS image as well as the contribution of the neighbor pixels into the radiance registered at the sensor, smooths the discriminative features of the plastic material while they enhance water spectra features. Plastic spectra extracted from the pan-sharpened HS image

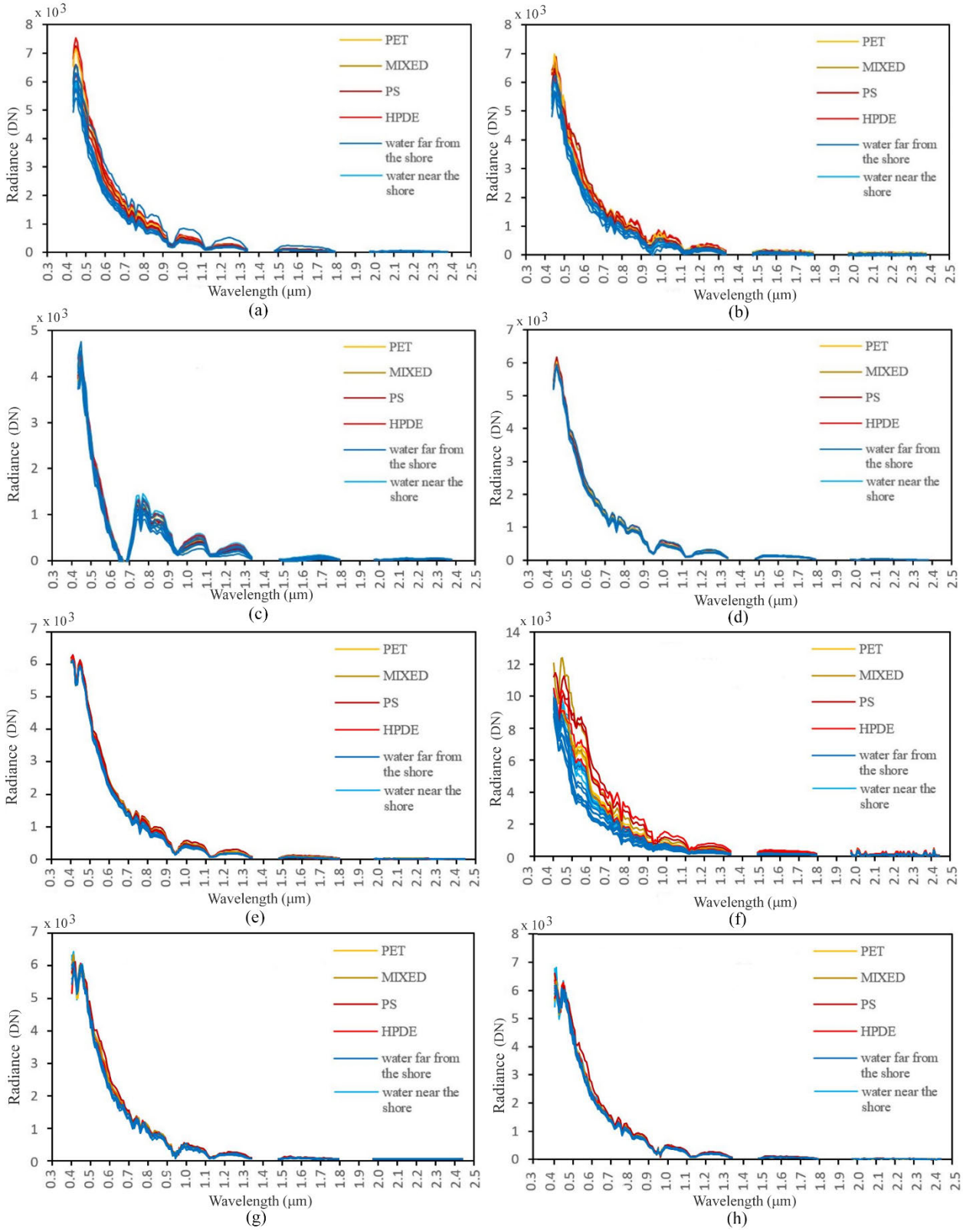

FIGURE 5. Spectral signatures of water and plastic targets. (a) LMM. (b) LMVM. (c) BayesNaive. (d) HySure. (e) PNN. (f) PNN-histogram clipping. (g) CAE. (h) GDD.

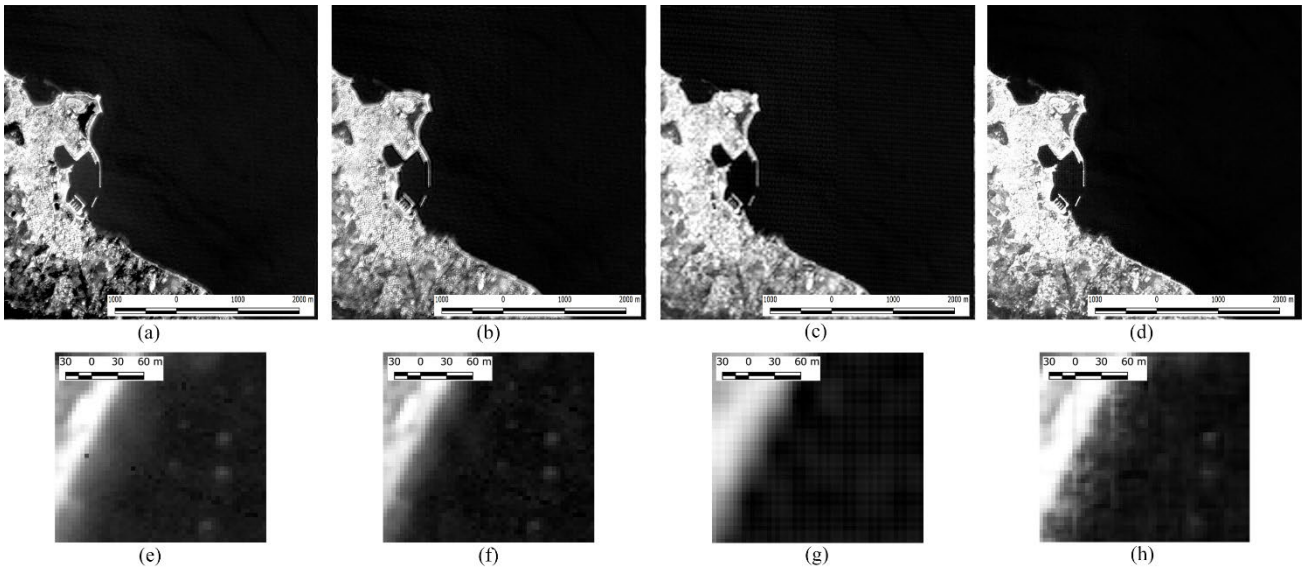

FIGURE 6. Pansharpening results for the PRISMA image acquired on 18/9/2020 (zoomed out and zoomed in view) (670 nm). (a, e) PCA. (b, e) SFIM. (c, g) BayesNaive. (d, h) PNN – histogram clipping.

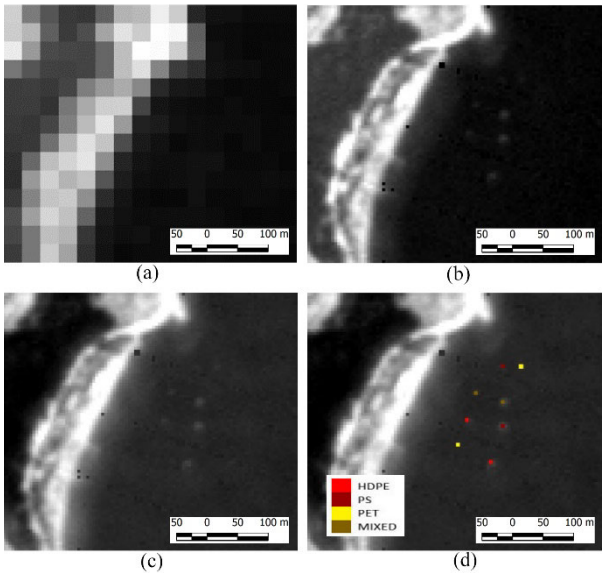

FIGURE 7. Pansharpening of the PRISMA image acquired on 18/9/2020. (a) Original HS image (670nm). (b) Panchromatic image. (c) Pan-sharpened PCA image (670nm). (d) Pan-sharpened PCA image (670nm) with plastic target marks.

present significant similarities to water spectra with crests and troughs in the same wavelengths. However, for plastics, crests present higher radiance values than for water due to the injection of the panchromatic image in the 30 m resolution HS image.

Thus, in this study, the proposed indexes for discriminating plastic targets from water are based on radiance differences between spectrum crests and troughs in the VNIR region, since water absorption in the SWIR bands significantly affects the spectra of the plastic objects in the sea. It was observed that three such differences efficiently discriminate differences in the same wavelengths but not of the same magnitude. A set of three indexes has been proposed that poses three different criteria to assign high probabilities to pixels that present plastic material. The first index was proposed after the observation of a diagram (Fig. 8) created by the formula written below (4):

$$\text{Index}_1 = R_i^2 - R_j \tag{4}$$

where $R_i \in [749.8, 781, 866, 988.4, 1088.6]$ nm: bands where high peaks are observed in the plastic spectra, and $R_j \in [951\text{ nm}]$: the band where the most significant trough is observed.

At 1120.5 nm very low radiance values are also observed but this band was not selected because it is significantly affected by atmospheric water vapor absorption. Fig. 8 presents the values of the first index, which has been calculated from the radiance spectra of the 18/09/2020 PCA pan-sharpened PRISMA image, using a different R_i band every time. Numbers 1-5 correspond to the preceding R_i band sequence, respectively. In order to achieve a comparable Y scale on the graph (Fig. 8), combinations 1, 2, and 3 were divided by 1000 and combinations 4 and 5 by 400. Based on the Euclidean distances between the most neighboring water and plastic spectra, the second combination, $R_i = 781$ nm and $R_j = 951$ nm, was selected as the most suitable because for this combination the two neighbor signatures exhibit the maximum distance. This index exploits discrimination characteristics of plastic spectra in the NIR.

To improve the correct detection of floating plastic material through indexes, incorrectly detected non-plastic pixels that remained after applying index_1, were sampled from the PCA pan-sharpened image of 18/09/2020 PRISMA acquisition, and their radiance signatures were observed (Fig. 9).

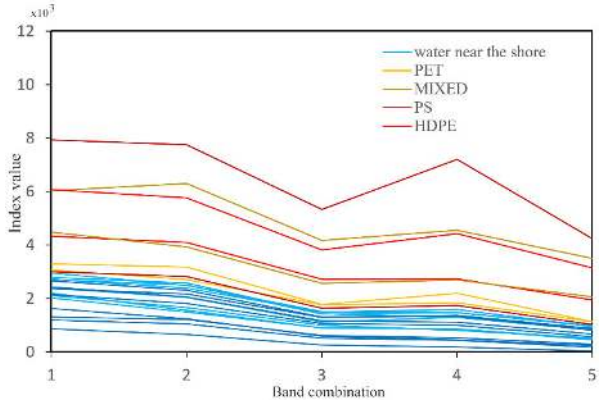

FIGURE 8. Combinations of the 1st proposed index for the PCA pan-sharpened image of the PRISMA data collected on 18/09/2020.

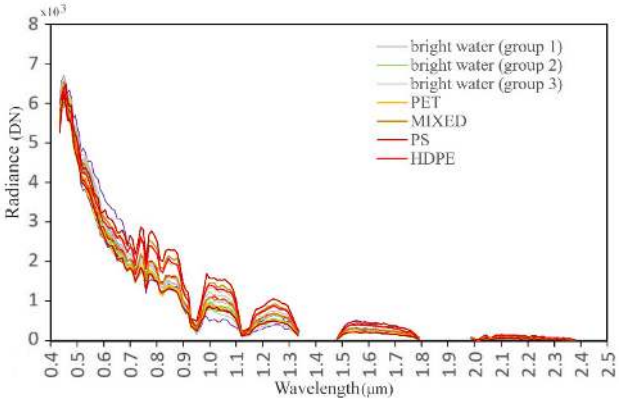

FIGURE 9. Radiance signatures of the plastic targets and the sampled bright water pixels not detected by the proposed 1st index. The spectra were extracted from the PCA pan-sharpened image of the PRISMA data collected on 18/09/2020.

The sampled spectra were divided into three groups according to the magnitude level of their radiance. Group 3 showed the highest radiance values, followed by groups 2 and 1. From the observation of the radiance signatures, it can be seen that the spectra from all three groups are mixed with the spectra of the targets. The same conclusion is derived when implementing the proposed index$_1$ (Fig. 10).

However, a possible separation was noticed in the visible part of the spectrum, which led to developing the second and third proposed indexes. The formula of the second proposed index is (5):

$$\text{Index}_2 = R_i^2 - R_j^2 \tag{5}$$

The second proposed index was implemented for the 10 combinations of bands that are presented in Table 2. For comparable Y scaling on the graph of Fig. 11, combinations 1-7 were divided by 10 000 and combinations 8-10 by 7000. In this graph, it can be observed that combination number 7 (bands: 596 nm and 719 nm) manages to separate the third group of the sampled bright water pixels from all the targets.

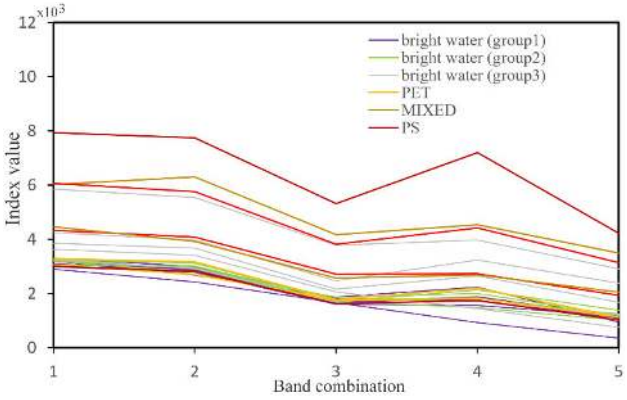

FIGURE 10. Implementation of the 1st proposed index on the radiance signatures of sampled bright water pixels that were not detected by this index. The spectra were extracted from the PCA pan-sharpened image of the PRISMA data collected on 18/09/2020.

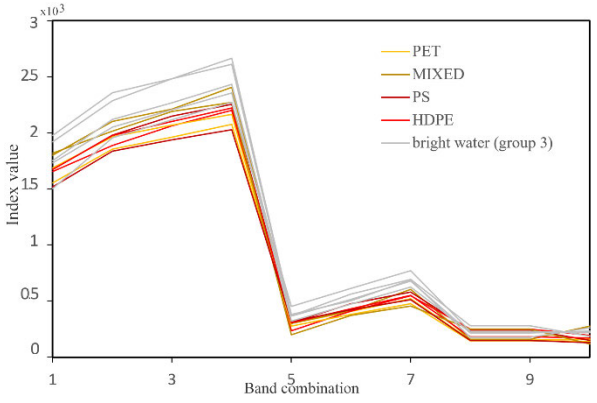

FIGURE 11. Combinations of the 2nd proposed index for the PCA pan-sharpened image of the PRISMA data collected on 18/09/2020. Separation of the third group of bright water sampled pixels in combination number 7.

TABLE 2. Combinations of bands that were tested for the 2nd proposed index.

combo / band	1	2	3	4	5	6	7	8	9	10
i	492				596			650		690
j	596	650	690	719	650	690	719	690	719	719

The formula of the third proposed index is presented below (6):

$$\text{Index}_3 = R_i - R_j \tag{6}$$

Similarly to index$_2$, the third proposed index was implemented for the 10 combinations of bands that are presented in Table 2. From the respective diagrams which are illustrated in Fig. 12, it can be observed that combination number 4 (bands: 492 nm and 719 nm) manages to separate group 1 and group 2 of the sampled bright water pixels from all the targets.

Finally, a combination of the previously mentioned indexes has been tested. The three indexes are applied independently on the pan-sharpened image after masking out the land

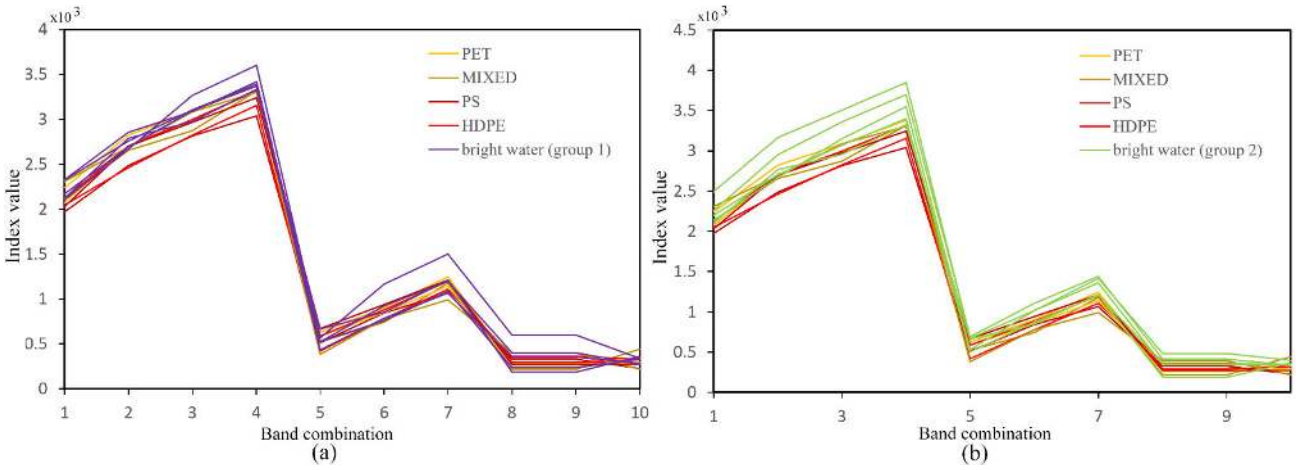

FIGURE 12. Combinations of the 3rd proposed index for the PCA pan-sharpened image of the PRISMA data collected on 18/09/2020. (a) Separation of 1st group of bright water sampled pixels in combination number 4. Separation of 2nd group of bright water sampled pixels in combination number 4.

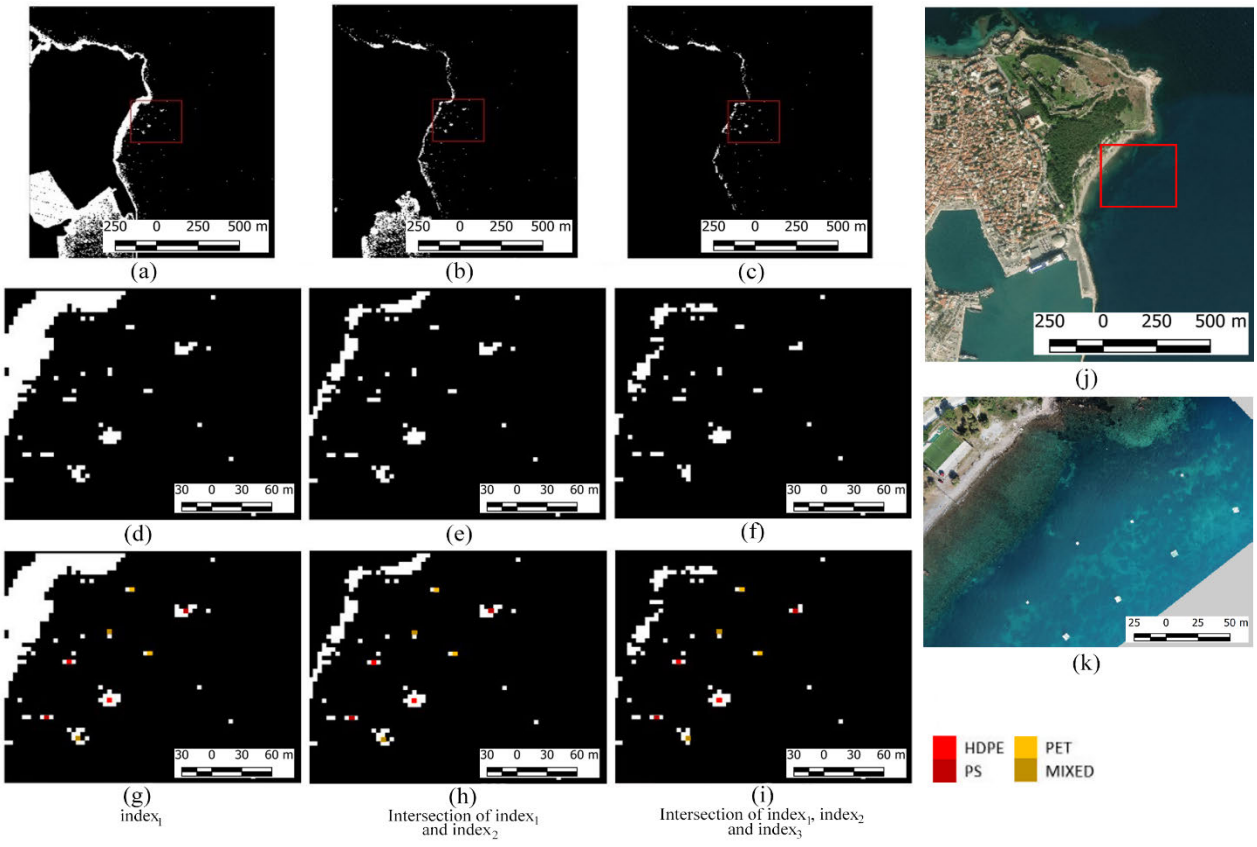

FIGURE 13. (a-c) Sequential application of the 3 indexes on the PCA pan-sharpened image of the PRISMA data collected on 18/09/2020 (land is removed). (d-f) Detail of a-c images over the area of the plastic targets. (g-i) Detail of a-c images over the area of the plastic targets with highlighted targets. (j) Google Earth image. (k) Orthophoto of the targets.

region. Then the final output is produced as the intersection of the individual results. Thus, the order of the implementation of the indexes is irrelevant. In each index output, a threshold is set, enabling the creation of a simplified detection and quantification algorithm. Indicative threshold values are: 1) for the first two index images: [mean value of the image] + 2.20 × [standard deviation of the image] and 2) for the third index image: [mean value of the image] − 0.60 × [standard deviation of the image]. The results after implementing the indexes on the PCA pan-sharpened images derived

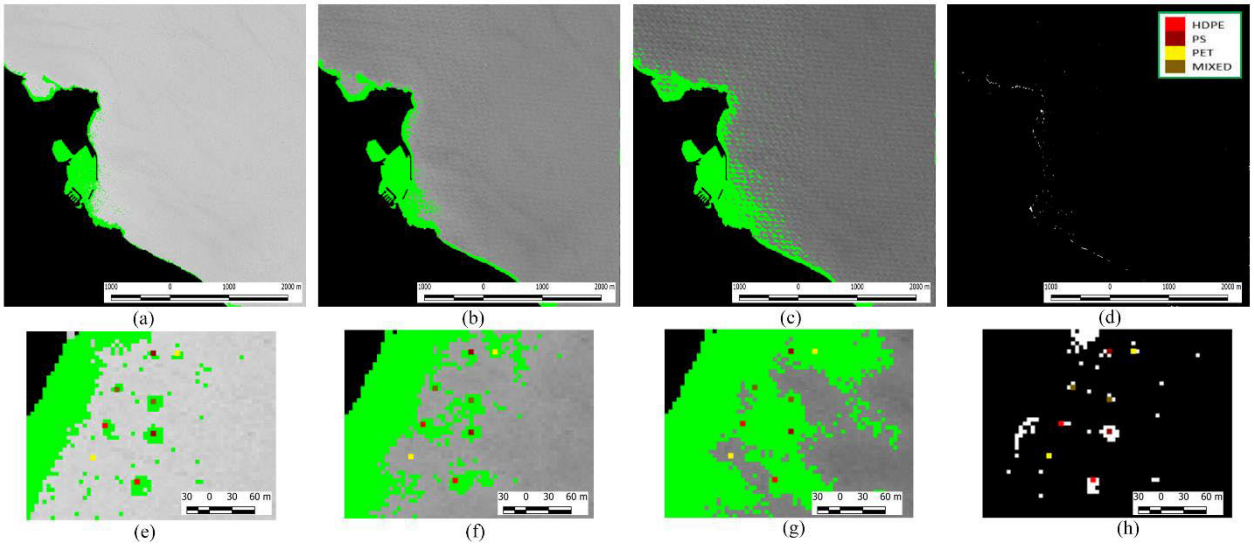

FIGURE 14. Zoomed out and zoomed in view of the area of the experiment of the PRISMA data collected on 18/09/2020. (a, e) Panchromatic image. (b, f) Total suspended matter (TSM) map. (c, g) Chl-a concentration map. (d, h) The intersection of the proposed indexes. Plastic targets are highlighted with colors in images e-h. For the PAN, TSM, and Chl-a images, green color defines the values found in the range of the target values. The land has been masked out.

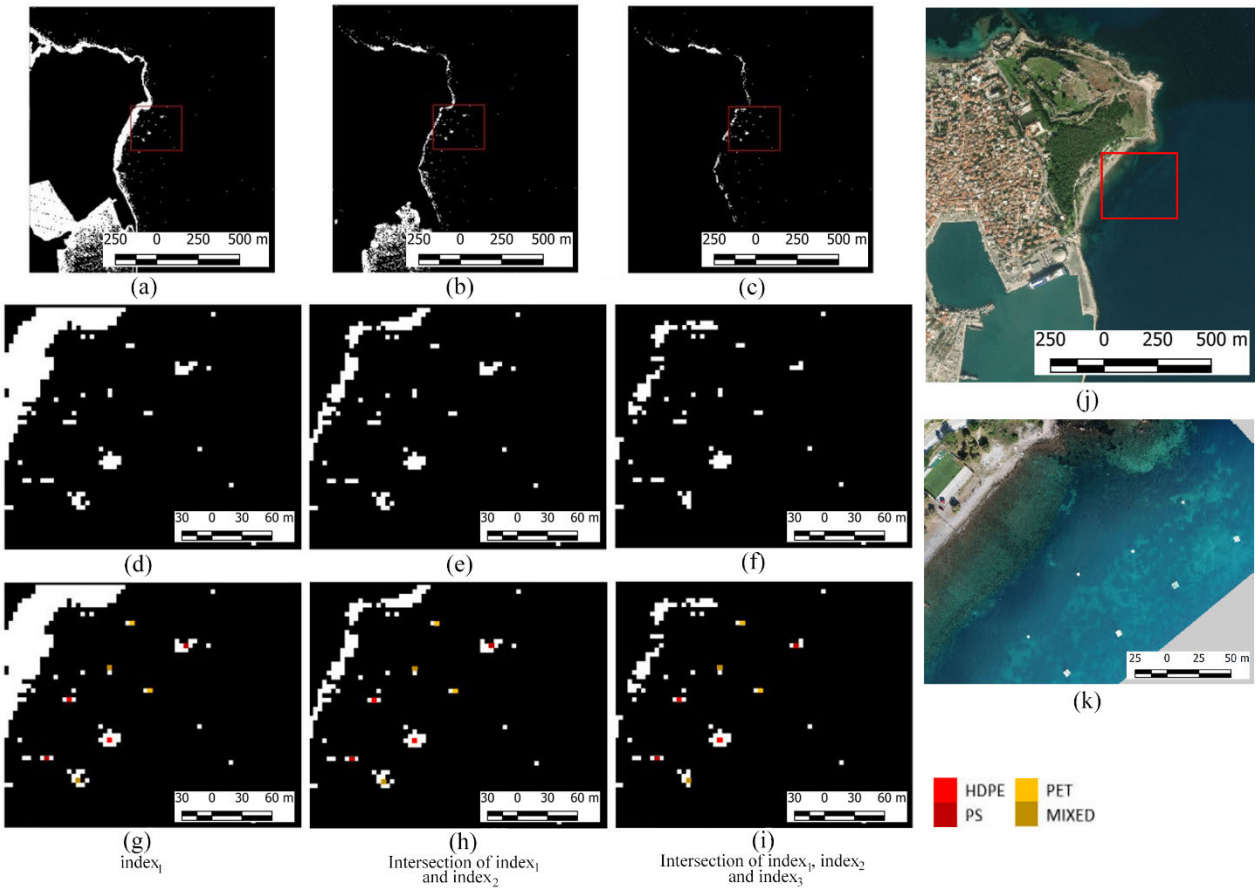

FIGURE 15. (a-c) Sequential application of the 3 indexes on the PCA pan-sharpened image of the PRISMA data collected on 22/10/2020 (land is removed). (d-f) Detail of a-c images over the area of the plastic targets. (g-i) Detail of a-c images over the area of the plastic targets with highlighted targets. (j) Google Earth image. (k) Orthophoto of the targets.

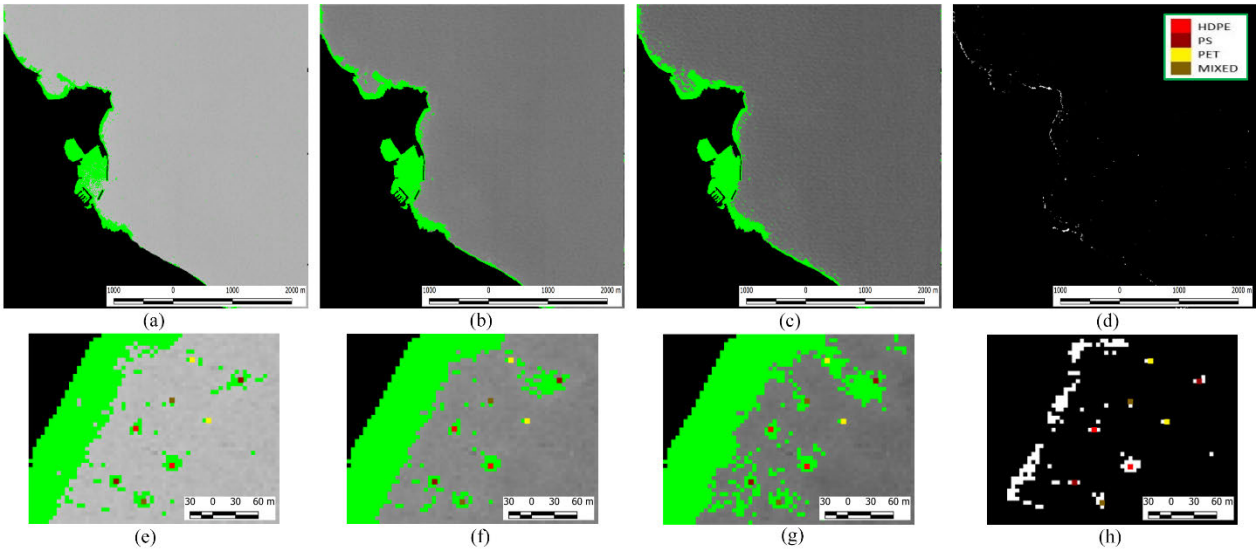

FIGURE 16. Zoomed out and zoomed in view of the area of the experiment of the PRISMA data collected on 22/09/2020. (a, e) Panchromatic image. (b, f) Total suspended matter (TSM) map. (c, g) Chl-a concentration map. (d, h) The intersection of the proposed indexes. Plastic targets are highlighted with colors in images e-h. For the PAN, TSM and Chl-a images, green color defines the values found in the range of the target values. The land has been masked out.

from the PRISMA acquisitions of dates: 18/09/2020 and 22/10/2020 are depicted in Fig. 13 and Fig. 15 respectively. The white color shows the pixels with a high probability of being plastic material (Figs. 13 (d-f), 15 (d-f)). In Figs. 13 (g-i), 15 (g-i) the plastic targets are shown with colors. In the image of the intersection of the three indexes it is observed that incorrectly detected bright non-plastic pixels are very limited and most of them situated less than 30 m from the coastline, where seabed contributions are very high. It should be noted that only a few remaining bright non-plastic pixels are presented at the deeper water areas. These are mainly related to remaining noise after the filtering of the PAN image. In Figs. 14, 16 the panchromatic PRISMA image (Figs. 14 (a, e), 16 (a, e)), the total suspended matter (TSM) index [35] (Figs. 14 (b, f), 16 (b, f)), and the OC4Me Chl-a concentration index [36] (Figs. 14 (c, g), 16 (c, g)), are defined according to the range of the target values. It can be seen that the plastic targets cannot be detected solely by the panchromatic PRISMA image as they are confused with other materials in the seabed or on the sea surface. It is also shown that even though the target pixels show high concentrations of suspended matter and chlorophyll, using the intersection of the proposed indexes (Figs. 14 (d, h), 16 (d, h)), the detection of the plastic targets is quite accurate with only a few pixels (most of them very close to the coast) being erroneously indicated as plastic materials.

VI. CONCLUSION

In this study, evaluation of PRISMA imagery potentials for marine plastic litter detection has been carried out for the first time. To our knowledge, it is also the first attempt to investigate this problem via satellite hyperspectral imagery. The study focuses on the detection of small-sized targets ($\leq$5 m) which is even more challenging. To this end, the required pre-processing steps, such as fine co-registration of PAN and HS images and elimination of the observed noise in the PAN image have been defined. A new algorithm has been developed to eliminate the periodic noise which is observed on the PRISMA PAN images. Several pansharpening approaches and methods have been applied and evaluated for their ability to spectrally discriminate plastics from water as well as for their spatial distortions. Among them, the component substitution methods yielded the best results. Especially, the simple PCA-based substitution efficiently separates plastic spectra from water without producing blurry and duplicate edges or pixelation in the produced image. In the pan-sharpened image, plastic targets with size 5.1 m $\times$ 5.1 m and 2.4 $\times$ 2.4 m are easily detected, while targets with size 0.6 m $\times$ 0.6 m cannot be detected. The size of the observed pieces is equivalent to the 8% pixel coverage of the original HS image. However, it would be interesting to conduct further experiments to see which is the minimum size of the target (or minimum coverage of the PRISMA HS pixel) to allow to acquire distinguishable plastic spectral features. As a start, the spectrum from a pure plastic pixel (e.g. greenhouse) could be considered. This minimum would be important in the context of discrimination versus other non-plastic floating materials.

Among plastic materials, transparent and green PET polymer is the most difficult to be detected. Discriminating transparent and green PET polymer is even challenging for targets with 5.1 m $\times$ 5.1 m size. In contrast, HDPE and PS polymers as well as the mixed composition of the three materials can be easily detected. Spectra of all plastic materials derived by the

pan-sharpened images present similarities with water spectra. The water abundance within the pixel coverage of the HS image and the contribution of the neighbor pixels into the radiance registered at the sensor, smooth the discriminative features of the plastic material, particularly in the SWIR region where water absorption is very high. Pansharpening injects spatial information from the PAN image in the HS image; however, it cannot enhance the absorption features of the plastic materials. The influence of seawater on ocean plastic spectra is preserved and consequently features observed in the laboratory and airborne-based spectra [37] are not apparent in the derived spectral signatures. However, some spectral characteristics observed in the VNIR region can be exploited for producing marine plastic indexes. These characteristics rely on the magnitude of the radiance differences between crests and troughs along the VNIR region of the spectra that plastic materials present.

The observed spectral characteristics led to the development of three indexes that can adequately detect plastic material with a few false alarm signals on PRISMA pan-sharpened data. VNIR bands with central wavelengths at (492, 596, 719, 781, and 951) nm are used for the calculation of these indexes. The indexes set three different criteria in order to assign high probabilities to pixels that present plastic material. A methodology that is based on the combination of the three developed indexes led to very interesting results for the detection of plastics on seawater. The targets were identified as suspended matter and chlorophyll-a by the TSM and OC4Me indexes, however, the proposed plastic indexes and the index combining methodology successfully recognized them from the non-plastic materials. The next step is to compare the results with other non-plastic floating materials (e.g. floating vegetation and foam), in view to demonstrate that PRISMA could be used as a stand-alone satellite to detect the likelihood of plastic presence. Targets of vegetation might also be used in future experiments to examine if they are distinguishable from plastic targets.

ACKNOWLEDGMENT

This work was implemented in the framework of the project REACT.

REFERENCES

[1] J. R. Jambeck, R. Geyer, C. Wilcox, T. R. Siegler, M. Perryman, A. Andrady, R. Narayan, and K. L. Law, "Plastic waste inputs from land into the ocean," *Science*, vol. 347, no. 6223, pp. 768–771, Feb. 2015.

[2] L. Lebreton, B. Slat, F. Ferrari, B. Sainte-Rose, J. Aitken, R. Marthouse, S. Hajbane, S. Cunsolo, A. Schwarz, A. Levivier, K. Noble, P. Debeljak, H. Maral, R. Schoeneich-Argent, R. Brambini, and J. Reisser, "Evidence that the great pacific garbage patch is rapidly accumulating plastic," *Sci. Rep.*, vol. 8, no. 1, Dec. 2018, Art. no. 4666.

[3] M. Carbery, W. O'Connor, and T. Palanisami, "Trophic transfer of microplastics and mixed contaminants in the marine food Web and implications for human health," *Environ. Int.*, vol. 115, pp. 400–409, Jun. 2018.

[4] L. M. Rios, C. Moore, and P. R. Jones, "Persistent organic pollutants carried by synthetic polymers in the ocean environment," *Mar. Pollut. Bull.*, vol. 54, no. 8, pp. 1230–1237, Aug. 2007.

[5] S. Casabianca, S. Capellacci, M. G. Giacobbe, C. Dell'Aversano, L. Tartaglione, F. Varriale, R. Narizzano, F. Risso, P. Moretto, A. Dagnino, R. Bertolotto, E. Barbone, N. Ungaro, and A. Penna, "Plastic-associated harmful microalgal assemblages in marine environment," *Environ. Pollut.*, vol. 244, pp. 617–626, Jan. 2019.

[6] *Guidelines for the Monitoring and Assessment of Plastic Litter in the Ocean*, GESAMP, London, U.K., 2019.

[7] *United Nations Transforming Our World: The 2030 Agenda for Sustainable Development. A/RES/70/1*, UN, New York, NY, USA, 2015.

[8] *Directive 2008/56/EC*, Eur. Parliament Council Eur. Union, Strasbourg, France. [Online]. Available: https://eur-lex.europa.eu/legal-content/EN/TXT/PDF/?uri=CELEX:32008L0056&from=en

[9] T. Acuña-Ruz, D. Uribe, R. Taylor, L. Amézquita, M. C. Guzmán, J. Merrill, P. Martínez, L. Voisin, and C. B. Mattar, "Anthropogenic marine debris over beaches: Spectral characterization for remote sensing applications," *Remote Sens. Environ.*, vol. 217, pp. 309–322, Nov. 2018.

[10] S. P. Garaba and H. M. Dierssen, "An airborne remote sensing case study of synthetic hydrocarbon detection using short wave infrared absorption features identified from marine-harvested macro- and microplastics," *Remote Sens. Environ.*, vol. 205, pp. 224–235, Feb. 2018.

[11] K. Topouzelis, A. Papakonstantinou, and S. P. Garaba, "Detection of floating plastics from satellite and unmanned aerial systems (plastic litter project 2018)," *Int. J. Appl. Earth Observ. Geoinf.*, vol. 79, pp. 175–183, Jul. 2019.

[12] K. Topouzelis, D. Papageorgiou, A. Karagaitanakis, A. Papakonstantinou, and M. A. Ballesteros, "Remote sensing of sea surface artificial floating plastic targets with sentinel-2 and unmanned aerial systems (plastic litter project 2019)," *Remote Sens.*, vol. 12, no. 12, p. 2013, Jun. 2020.

[13] L. Biermann, D. Clewley, V. Martinez-Vicente, and K. Topouzelis, "Finding plastic patches in coastal waters using optical satellite data," *Sci. Rep.*, vol. 10, no. 1, Dec. 2020, Art. no. 5364.

[14] J. P. Matthews, L. Ostrovsky, Y. Yoshikawa, S. Komori, and H. Tamura, "Dynamics and early post-tsunami evolution of floating marine debris near Fukushima Daiichi," *Nature Geosci.*, vol. 10, no. 8, pp. 598–603, Aug. 2017.

[15] A. Kikaki, K. Karantzalos, C. A. Power, and D. E. Raitsos, "Remotely sensing the source and transport of marine plastic debris in bay islands of honduras (Caribbean Sea)," *Remote Sens.*, vol. 12, no. 11, p. 1727, May 2020.

[16] L. Loncan, L. B. de Almeida, J. M. Bioucas-Dias, X. Briottet, J. Chanussot, N. Dobigeon, S. Fabre, W. Liao, G. A. Licciardi, M. Simões, J.-Y. Tourneret, M. A. Veganzones, G. Vivone, Q. Wei, and N. Yokoya, "Hyperspectral pansharpening: A review," *IEEE Geosci. Remote Sens. Mag.*, vol. 3, no. 3, pp. 27–46, Sep. 2015.

[17] B. Aiazzi, S. Baronti, and M. Selva, "Improving component substitution pansharpening through multivariate regression of MS + Pan data," *IEEE Trans. Geosci. Remote Sens.*, vol. 45, no. 10, pp. 3230–3239, Oct. 2007.

[18] J. G. Liu, "Smoothing filter-based intensity modulation: A spectral preserve image fusion technique for improving spatial details," *Int. J. Remote Sens.*, vol. 21, no. 18, pp. 3461–3472, Jan. 2000.

[19] G. Vivone, R. Restaino, M. D. Mura, G. Licciardi, and J. Chanussot, "Contrast and error-based fusion schemes for multispectral image pansharpening," *IEEE Geosci. Remote Sens. Lett.*, vol. 11, no. 5, pp. 930–934, May 2014.

[20] V. Karathanassi, P. Kolokousis, and S. Ioannidou, "A comparison study on fusion methods using evaluation indicators," *Int. J. Remote Sens.*, vol. 28, no. 10, pp. 2309–2341, May 2007.

[21] W. Liao, X. Huang, F. Van Coillie, S. Gautama, A. Pizurica, W. Philips, H. Liu, T. Zhu, M. Shimoni, G. Moser, and D. Tuia, "Processing of multiresolution thermal hyperspectral and digital color data: Outcome of the 2014 IEEE GRSS data fusion contest," *IEEE J. Sel. Topics Appl. Earth Observ. Remote Sens.*, vol. 8, no. 6, pp. 2984–2996, Jun. 2015.

[22] Q. Wei, N. Dobigeon, and J.-Y. Tourneret, "Bayesian fusion of multispectral and hyperspectral images with unknown sensor spectral response," in *Proc. IEEE Int. Conf. Image Process. (ICIP)*, Oct. 2014, pp. 698–702.

[23] M. Simoes, J. Bioucas-Dias, L. B. Almeida, and J. Chanussot, "A convex formulation for hyperspectral image superresolution via subspace-based regularization," *IEEE Trans. Geosci. Remote Sens.*, vol. 53, no. 6, pp. 3373–3388, Jun. 2015.

[24] F. Chollet *et al.*, "Keras: The Python deep learning library," François Chollet, 2015. [Online]. Available: https://keras.io

[25] M. Abadi *et al.*, "TensorFlow: A system for large-scale machine learning," in *Proc. 12th USENIX Symp. Oper. Syst. Des. Implement. (OSDI)*, May 2016, pp. 1–21.

[26] A. Paszke *et al.*, "PyTorch: An imperative style, high-performance deep learning library," in *Proc. Adv. Neural Inf. Process. Syst.*, vol. 32, 2019, pp. 8026–8037.
[27] G. Masi, D. Cozzolino, L. Verdoliva, and G. Scarpa, "Pansharpening by convolutional neural networks," *Remote Sens.*, vol. 8, no. 7, p. 594, Jul. 2016.
[28] D. P. Kingma and J. Ba, "Adam: A method for stochastic optimization," in *Proc. 3rd Int. Learn. Represent. (ICLR)*, Dec. 2014, pp. 1–15.
[29] A. Azarang, H. E. Manoochehri, and N. Kehtarnavaz, "Convolutional autoencoder-based multispectral image fusion," *IEEE Access*, vol. 7, pp. 35673–35683, 2019.
[30] T. Uezato, D. Hong, N. Yokoya, and W. He, "Guided deep decoder: Unsupervised image pair fusion," in *Proc. Eur. Conf. Comput. Vis.*, in Lecture Notes in Computer Science: Including Subseries Lecture Notes in Artificial Intelligence and Lecture Notes in Bioinformatics, 2020, pp. 87–102.
[31] O. Ronneberger, P. Fischer, and T. Brox, "U-Net: Convolutional networks for biomedical image segmentation," in *Proc. Int. Conf. Med. Image Comput. Comput.-Assist. Intervent.*, in Lecture Notes in Computer Science: Including Subseries Lecture Notes in Artificial Intelligence and Lecture Notes in Bioinformatics, 2015, pp. 234–241.
[32] *Agisoft Metashape (Version 1.5.1)*, Agisoft LLC, Saint Petersburg, Russia, 2015.
[33] F. Kühn, K. Oppermann, and B. Hörig, "Hydrocarbon index—An algorithm for hyperspectral detection of hydrocarbons," *Int. J. Remote Sens.*, vol. 25, no. 12, pp. 2467–2473, Jun. 2004.
[34] D. Papageorgiou, "Floating plastic detection using sentinel-2 imagery," Diploma thesis, Nat. Tech. Univ. Athens, Athens, Greece, 2019.
[35] B. Nechad, K. G. Ruddick, and Y. Park, "Calibration and validation of a generic multisensor algorithm for mapping of total suspended matter in turbid waters," *Remote Sens. Environ.*, vol. 114, no. 4, pp. 854–866, Apr. 2010.
[36] M. S. Twardowski, H. Claustre, S. A. Freeman, D. Stramski, and Y. Huot, "Optical backscattering properties of the clearest natural waters," *Biogeosciences*, vol. 4, no. 6, pp. 1041–1058, Nov. 2007.
[37] S. P. Garaba, J. Aitken, B. Slat, H. M. Dierssen, L. Lebreton, O. Zielinski, and J. Reisser, "Sensing ocean plastics with an airborne hyperspectral shortwave infrared imager," *Environ. Sci. Technol.*, vol. 52, pp. 11699–11707, Sep. 2018.

MARIA KREMEZI received the M.S. degree in surveying engineering from the National Technical University of Athens (NTUA), Greece, in 2016, where she is currently pursuing the Ph.D. degree in remote sensing.

Since 2017, she has been a Researcher with the Laboratory of Remote Sensing, NTUA, participating in many EU projects in the field of multispectral and hyperspectral data processing. She is the author of publications in international scientific journals and proceedings of international conferences. During her Ph.D. studies, her research interests include hyperspectral remote sensing with emphasis on image fusion theory and techniques.

Ms. Kremezi received a 3-Year Scholarship from the NTUA Research Committee, in 2017.

VIKTORIA KRISTOLLARI received the M.S. degree in rural and surveying engineering from the National Technical University of Athens (NTUA), Athens, Greece, in 2016, where she is currently pursuing the Ph.D. degree in remote sensing.

Since 2017, she has been a Researcher with the Laboratory of Remote Sensing, NTUA, and has participated in EU projects. Her research concentrates on multispectral and hyperspectral image processing via artificial neural networks. She has authored publications for peer-reviewed international scientific journals and conferences.

Ms. Kristollari was a recipient of the Excellence Award of the Limmat Stiftung Foundation, in 2016, and was granted a 3-Year Scholarship by the NTUA Research Committee for her Ph.D. research, in 2017.

VASSILIA KARATHANASSI received the B.S. degree in rural and surveying engineering from the National Technical University of Athens (NTUA), Greece, in 1984, the M.S. degree in urban planning-geography from Paris V, France, in 1985, and the Ph.D. degree in remote sensing from NTUA, in 1990.

Since 2000, she has been a Professor with the School of Rural and Surveying Engineering, NTUA, specialized in hyperspectral/multispectral remote sensing and InSAR/DInSAR processing and applications. She teaches multiple undergraduate and postgraduate courses and she has supervised more than 40 undergraduate, eight master's theses, eight Ph.D. theses (four of them completed), and one postdoctoral research. Her published research work includes more than 100 articles and one chapter in the book *Hyperspectral Remote Sensing*. Furthermore, she is involved in EU and national excellence/competitive research projects as a Coordinator, a Principal Investigator, and a Researcher toward the design, development, and validation of state-of-the-art methodologies, and cutting-edge technology in remote sensing and earth observation.

KONSTANTINOS TOPOUZELIS (Member, IEEE) received the B.S. degree in environmental studies from the Department of Environment, University of the Aegean, Greece, in 1999, the M.S. degree in remote sensing from the Department of Applied Physics and Mechanical Engineering, University of Dundee, U.K., in 2000, and the Ph.D. degree in pollution monitoring in space from the School of Rural and Surveying Engineering, National Technical University of Athens, in 2007.

He is currently an Assistant Professor with the Department of Marine Sciences, University of the Aegean, where he is leading the Marine Remote Sensing Group. His main research interest is on the analysis of remote sensing datasets, including satellite and aerial images, for marine and coastal applications. His expertise includes the automatic detection of oceanographic phenomena, object-based image analysis, image processing algorithms, and coastal mapping. He has been a member of the IEEE Geoscience and Remote Sensing Society, since 2013, and he is the author of more than 40 refereed articles in international scientific journals and books, a member of the editorial board in several scientific journals, and the principal investigator in international research projects. Prior to his academic career, he worked for the European Commission Joint Research Centre.

POL KOLOKOUSSIS received the M.S. degree in rural and surveying engineering and the Ph.D. degree in remote sensing from the National Technical University of Athens (NTUA), Greece, in 1993 and 2008, respectively.

Since 1993, he has been a Research Assistant with the Laboratory of Remote Sensing, School of Rural and Surveying Engineering, NTUA, where he has been a Teaching Associate, since 2002. During the last years, his research interests include acquisition and processing of hyperspectral and thermal remote sensing imagery, the development of algorithms and methods for the analysis of remote sensing data, and object-based image analysis, with emphasis on techniques used for identifying changes and protecting the natural environment. He has published work in several international journals and conferences, has participated in more than 25 National and European Research Projects, and is a reviewer in a range of international journals.

NICOLÒ TAGGIO received the B.S. degree in mathematics and the M.S. degree in applied mathematics from the University of Bari, Italy, in 2016.

From 2016 to 2018, he was a Software Analyst and a Developer of the SpaceStream Strategic Business Unit, Planetek Italia s.r.l., where he has been a Data Scientist and an AI Researcher of the Geo Analytics Team, since 2018. He collaborates in many different projects, mainly financed by the European Space Agency. His research interests include machine learning and deep learning for Earth observation with a particular focus on the use of multispectral and hyperspectral images. His main expertise concerns object detection, semantic segmentation, land cover classification, time series analysis, change detection, and anomaly detection.

ANTONELLO AIELLO received the B.S. degree in civil engineering and the M.S. degree in environmental engineering from the Polytechnic University of Bari, Italy, in 2007 and 2011, respectively, and the Ph.D. degree in Earth sciences from the University of Basilicata, Italy, in 2017.

He has more than ten years of experience in GIS and EO by remote sensing. During his master studies, he worked on the use of satellite TIR data for monitoring the spatial and temporal distribution of SST. He also developed an object-based classification procedure from VHSR air- and satellite-borne data aimed at plastic-covered vineyard extraction. During the Ph.D. program, his research activity concerned the analysis of coastal dynamics and vulnerability to erosion, as well as soil erosion and degradation in coastal basins, with techniques that encompass Earth observation by remote sensing, GIS, geoprocessing, and spatial analysis and modeling. He published articles on leading international peer-reviewed journals and presented work in national and international conferences. After a period as an External Consultant at the Joint Research Centre of the European Commission (Institute for Space, Security and Migration-Disaster Risk Management Unit), he joined Planetek Italia s.r.l., in 2017, where he is currently a Senior Technical Specialist for both the Rheticus® Team and the Geospatial Application Team. He deals with the design/development of geoservices, writing proposals in response to ITT by European Agencies, and project management. He is the Project Manager of the ESA-funded REACT project—"Crowdsourcing, Copernicus and Hyperspectral Satellite Data for Marine Plastic Litter Detection, Quantification and Tracking."

GIULIO CERIOLA received the B.S. degree in physics and the first level master's degree in technologies for remote sensing from space from the University of Bari, Italy, in 1998 and 2003, respectively.

From 2003 to 2005, he worked at Telespazio for developing applications that process EO data to gather land and temperature products and indexes. Since 2005, he has been working with Planetek Italia s.r.l., on environment application fields focusing on advanced EO processing techniques for land and water applications using both optical and SAR data. He is involved in international projects with European and national agencies, related to the monitoring of the water quality of inland and sea areas, and land use and land cover applications. Since 2019, he has been the Head of the Geo-Analytics Design Team, Planetek Italia, pushing the most advanced and state-of-the-art solutions for providing added-value products and services based on remote sensing data (optical and SAR) and other geospatial information.

ENRICO BARBONE received the B.S. degree in natural science from the University of Bari, Italy, in 2002, the M.S. degree in environmental monitoring from the University of Lecce, Italy, in 2004, and the Ph.D. degree in ecology from the University of Salento, Italy, in 2008.

He was a Research Assistant with the Ecology Laboratory, University of Lecce, working on the definition of scientific methods for environmental policy support for the application of Water Framework Directive (2000/60/CE) and also a Scientific Officer at DG JRC, Institute for the Environment and Sustainability, working on the Marine Strategy Framework Directive (2008/56/EC). He is the coauthor of more than 30 articles in international peer-reviewed journals and technical guidelines. Since 2011, he has been working as an Environmental Officer at the Regional Environmental Protection Agency of the Apulia region, where he is responsible for the coordination of the monitoring campaign within the application of the water framework directive and marine strategy framework.

PAOLO CORRADI received the M.S. degree in electronic engineering from the University of Parma, Italy, in 2002, and the Ph.D. degree in microsystems engineering from the Tor Vergata University of Rome, Italy, in 2007.

From 2009 to 2014, he was a System Engineer at the International Space Station, Directorate of Human Spaceflight and Exploration of the European Space Agency (ESA), for the development of payloads. Since 2015, he has been an Optical System Engineer at the Mechatronics and Optics Division, Optics Section, Directorate of Technology, Engineering and Quality, ESA/ESTEC, Noordwijk, The Netherlands, for the development of satellite optical instruments and technologies. He is currently coordinating the ESA Discovery Campaign on Remote Sensing of Plastic Marine Litter.